Introducing Virtual DIC to Remove Interpolation Bias and Process Optimal Patterns

Y. Shi, B. Blaysat, Hélène Chanal, M. Grédiac

Introducing Virtual DIC to remove interpolation bias and process optimal patterns

Yiheng Shi, Benoît Blaysat[1], Hélène Chanal and Michel Grédiac

Université Clermont Auvergne, Clermont Auvergne INP, CNRS, Institut Pascal, Clermont-Ferrand, F-63000, France.

Contributing authors: benoit.blaysat@uca.fr;

Abstract

Background: Digital Image Correlation (DIC) is an image-based measurement technique routinely used in experimental mechanics, which provides displacement and strain maps of an observed surface/volume. The metrological performance of DIC has reached its limit which is directly determined by the texture of the imaged surface/volume. Objective : This paper proposes a novel DIC strategy, which relies on a virtual image. This image, noiseless and of infinite resolution, is moreover optimized for providing measurements with the best metrological performance. Methods : The so-called Virtual DIC retrieves the displacement fields by comparing this virtual image to the experimental images. No interpolation is required and processing optimal textures such as checkerboards is possible. Results : Virtual DIC is first applied on synthetic images for comparison purposes with a usual DIC approach. Outstanding metrological performance is observed thanks to the possibility of processing checkerboard patterns. Conclusions : The proposed Virtual DIC is twofold: (i) thanks to the use of a closed-form expression, built-in DIC operators are elaborated without recurring to noisy and poorly defined real images. Interpolation is therefore avoided; (ii) it makes possible it to process checkerboard patterns, which offers the best metrological performance.

keywords

Digital Image Correlation, DIC, metrology, full-field measurement, checkerboard patterns

1 Introduction

Introduced in the eighties by Sutton [1] in experimental mechanics, Digital Image Correlation (DIC) is a measurement technique nowadays routinely used. It is an image-based approach that provides fields of mechanical information such as displacement fields, contrary to pointwise sensors like strain gauge or extensometer. The domain of interest of the specimen surface is imaged, and local gray level distributions are tracked to retrieve the physical displacement that deforms the observed texture. Initial applications relied on the use of single camera systems and measurements were therefore limited to 2D cases. Generalizations exist for multi-camera systems [2–5] that measure 3D displacement of surfaces. Tomography extends DIC to 3D bulk measurements [6, 7]. Algorithmic aspects of DIC have been discussed in parallel with the progress of image acquisition system. Researchers from the community of experimental mechanics naturally extended well-known tools of the computer vision community to their specific cases [8, 9]. Sub-pixel and small strain measurements featuring mastered metrological performance are indeed required when DIC is used for material characterization purposes. Consequently, the assessment and improvement of the metrological performance of DIC is nowadays a topical subject [10–32]. In particular, algorithmic aspects are thoroughly studied to elaborate closed-form expressions that link inputs, *i.e.* images, to outputs, *i.e.* displacement and strain maps, provided by DIC [19, 21, 29]. For instance, DIC can be modelled as a Savitzky-Golay low-pass filter [10]. The effect of interpolation [20] or of noise propagation from sensor to displacement maps [21] has also been thoroughly studied. The effect of the pattern itself on displacement or strain maps has been recently investigated. This effect has

been named "Pattern-Induced Bias" (PIB) in Ref. [30]. It traduces the interplay between image gradient and undermatched subset shape functions. The interested reader can refer to [29] for a consistent and complete model of biases affecting DIC. The entire chain acquisition and processing chain, from the surface texture to the displacement maps through the camera sensor is modelled in this reference.

The metrological performance of DIC mainly originates from two contributions, which are the signal carrier itself, *i.e.* the image texture, and its processing, *i.e.* the DIC algorithmic. To the best of the author's knowledge, optimizing DIC algorithmic is nowadays reaching its limit, and current studies aim to investigate its application to complex contexts, such as machining [33] or tomography [7, 34]. Indeed, when they are all applied to the same pattern, the main DIC techniques provide measurements with metrological performances of the same order of magnitude [32]. The focus shall thus be on the signal carrier, in other words on the pattern deposited onto the specimen surface. Recent progress in pattern engraving machines makes it possible to deposit one's own pattern [35], and helps investigate pattern optimization for DIC measurement [24, 31, 36–38]. For 2D measurement, checkerboard patterns stand out from the crowd when considering metrological performance [24, 37, 39]. Its high image gradient ensures low sensor noise propagation [37, 39, 40]. As demonstrated using synthetic data in [37], the RMSE (root mean square error, which includes random and systematic errors) decreases by a factor lying between 7 and 8 when switching from a classic random speckle pattern to a checkerboard pattern. In addition, pattern isotropy and periodicity contribute to reducing PIB [29, 30]. Such checkerboard patterns can be easily processed by a spectral technique such as Localized Spectrum Analysis (LSA) [41]. Nevertheless, pattern periodicity traps DIC in local minima and researchers have proposed to depreciate the pattern to resolve this problem [37, 42, 43].

In this context, the motivation behind the present paper is twofold:

- A new DIC formulation is introduced. It relies on a virtual image. This concept is inspired by the "Virtual Image Correlation" (VIC) introduced in [44], but which is limited to shape measurement. The VIC formulation proposed here is completely revisited, for providing full-field kinematic data, such as displacement and strain maps. The so-called Virtual DIC relies on the closed-form expression of the virtual image. Built-in DIC operators are thus elaborated without resorting to noisy and poorly defined images. Moreover, no interpolation is necessary thanks to the infinite resolution of the virtual image.
- It will be shown that Virtual DIC is able to correctly process checkerboard patterns without being trapped in local minima. Outstanding metrological properties are therefore observed.

Finding a tradeoff between the easiness of the speckle pattern depositing procedure and the metrological performance that is achieved is not an easy task. Nevertheless, for the common scale of observation, *i.e.* for specimens with sizes of about some centimeters in dimension, depositing optimized patterns is quite easy and fast with the laser engraving technique. Hence it makes sense to couple Virtual DIC with such patterns since Virtual DIC relies on a virtual image that resembles at best to the pattern which is deposited on the specimen.

The paper is organized as follows: the first section presents the methods. The Virtual DIC novelty is introduced and its use for processing checkerboard images is detailed. The second section illustrates the first implementation of Virtual DIC on synthetic images. Metrological performance is also assessed. A comparison with a classic subset-based DIC approach is made. Several studies have already concluded on the major gain offered by considering checkerboard patterns instead of speckle patterns. In addition, and contrary to random speckle patterns, checkerboard is described by a simple closed-form expression, which is a real asset for easily defining virtual images. Consequently, only checkerboard patterns are considered in this study; The third section shows

the application of Virtual DIC on an experimental challenging case, namely the measurement of a displacement field around a crack.

2 Methods

2.1 Principle of Virtual DIC - General case

The proposed Virtual DIC resembles the Local version of DIC, which aims to compare two images, denoted here by I^0 and I^1, in order to retrieve displacement $\underline{\mathsf{u}}$ that distinguishes them. For each pixel $\underline{\mathsf{x}}_\mathsf{p}$ of the Region of Interest (RoI), regularization is introduced and the problem is typically reformulated for a functional space $\mathcal{U}$ as the minimisation of the Sum Square Difference (SSD) over a domain $\omega_{\underline{\mathsf{x}}_\mathsf{p}}$ usually called subset. The RoI is defined in the reference state, which is captured by image I^0. Thus:

$$\forall \underline{\mathsf{x}}_\mathsf{p} \in \text{RoI}, \quad \underline{u}_{\text{DIC}}(\underline{\mathsf{x}}_\mathsf{p}) = \arg\min_{\underline{u}^* \in \mathcal{U}} \sum_{\underline{\mathsf{x}} \in \omega_{\underline{\mathsf{x}}_\mathsf{p}}} \left(I^0(\underline{\mathsf{x}}) - I^1\left(\underline{\mathsf{x}} + \underline{u}^*(\underline{\mathsf{x}})\right)\right)^2, \qquad (1)$$

where $\omega_{\underline{\mathsf{x}}_\mathsf{p}}$ corresponds to a squared domain of side $2 \times h + 1$ pixels centred on pixel $\underline{\mathsf{x}}_\mathsf{p}$, the test function $\underline{u}^*$ belongs to $\mathcal{U}$, which is defined here as a space of polynomial functions of degree p. In practice, the kinematic space $\mathcal{U}$ corresponds to the vector space determined by the set of n_{dof} subset shape functions $(\underline{\varphi}_i)_{1 \leq i \leq N_{dof}}$. It reads as follows:

$$\mathcal{U} = \text{span}\{(\underline{\varphi}_i)_{1 \leq i \leq N_{dof}}\}, \text{ or } \forall \underline{u}^* \in \mathcal{U}, \exists (u_i)_{1 \leq i \leq n_{dof}} \mid \underline{u}^* = \sum_{i=1}^{n_{dof}} u_i \underline{\varphi}_i. \qquad (2)$$

where $(u_i)_{1 \leq i \leq n_{dof}}$ are n_{dof} Degrees of Freedom (dof). More robust formulations have been introduced, such as the Normalized SSD or the Zero Normalized SSD. These formulations facilitate the convergence of the minimization scheme, but do not change the solution itself [17]. Moreover, the backward interpolation scheme used here has also been studied in the literature. Forward or mixed interpolation schemes have been introduced to reduce

interpolation bias or improve convergence, *e.g.* [45, 46]. In all existing formulations, images I^0 and/or I^1 are used for elaborating built-in operators or are interpolated for criterion evaluation. These images correspond to depreciated versions of the infinite resolution texture of the observed surface. They are indeed encoded by a finite discrete grid of pixels and are equal to integer numbers only because of the limited number of bits. Moreover, this quantification is impaired by sensor noise. The flowchart in Figure 1 summarizes the usual DIC approach and highlights impairments, which are the consequence of the use of discretized images. The principle of the Virtual DIC approach is also illustrated in this figure. The main idea of this technique consists in introducing a virtual image $\mathcal{I}$ defined through a closed-form expression. This image, which is perfectly known, will be used in the DIC process to avoid any handling of real images I^0 and I^1. Indeed, such handling might introduce extra information that might propagate to the displacement maps and might thus be considered as mechanical information. Consequently, Virtual DIC aims at avoiding the use of pre-processing such as filtering nor interpolating the images.

Equation (1) is thus written twice for determining the displacements from both real images I^0 and I^1 to the virtual image $\mathcal{I}$. These displacements are respectively referred to as $\underline{u}^0$ and $\underline{u}^1$ in the following. The physical displacement $\underline{u}$, which operates from real image I^0 to real image I^1 is then calculated from the two solutions of the preceding problem, as illustrated in Figure 2. This writes as follows:

$$\forall \underline{\mathtt{x}}_\mathtt{p} \in \mathrm{RoI}, \quad \underline{u}(\underline{\mathtt{x}}_\mathtt{p}) = \underline{u}^0(\underline{\mathtt{x}}_\mathtt{p}) - \underline{u}^1\left(\underline{\mathtt{x}}_\mathtt{p} + \underline{u}(\underline{\mathtt{x}}_\mathtt{p})\right), \tag{3}$$

where

$$\forall i \in \{0,1\}, \quad \underline{u}^i(\underline{\mathtt{x}}_\mathtt{p}) = \arg\min_{\underline{u}^* \in \mathcal{U}} \int_{\underline{x} \in \omega_{\underline{\mathtt{x}}_\mathtt{p}}} \left(I^i(\underline{x}) - \mathcal{I}\left(\underline{x} + \underline{u}^*(\underline{x})\right)\right)^2 \mathrm{d}\underline{x}, \tag{4}$$

where $\underline{u}^*$ denotes the test function. Note that the RoI is still defined in the reference state characterized by reference image I^0.

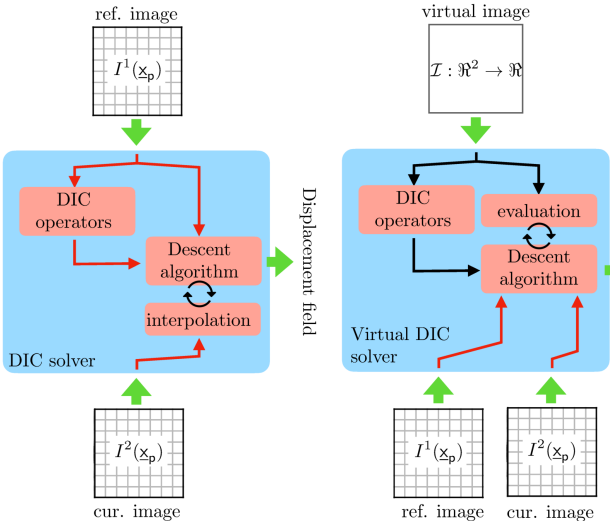

Fig. 1: Flowcharts summarizing classic DIC (left) and Virtual DIC (right). Red arrows correspond to data impaired by image acquisition noise and by quantization error. In classic DIC approaches, DIC operators are built up directly from real images, which are always noisy. These operators are therefore also impaired by noise. Moreover, for backward algorithms, the current image is interpolated. With Virtual DIC, DIC operators are directly defined with the closed-form expression of the virtual image. There is therefore no interpolation.

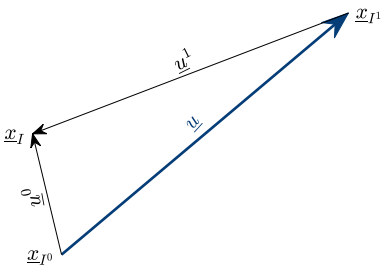

Fig. 2: Illustration of the displacements involved in Virtual DIC. Point $\underline{x}_{I^0}$ of image I^0 moves to point $\underline{x}_{I^1}$ of image I^1 through displacement $\underline{u}$. By introducing virtual image $\mathcal{I}$, displacement $\underline{u}^0$ traduces the movement of point $\underline{x}_{I^0}$ from I^0 to $\mathcal{I}$, and displacement $\underline{u}^1$ traduces the movement of point $\underline{x}_{I^1}$ from I^1 to $\mathcal{I}$. $\underline{u}$ is finally estimated by subtracting $\underline{u}^0$ and $\underline{u}^1$.

Because virtual image $\mathcal{I}$ is defined with a closed-form expression, Virtual DIC criteria defined in Equation (4) are written under their integral form and not as direct summations, like that involved in Equation (1). On the other hand, real images I^0 and I^1 are assumed to be constant within each pixel.

A usual Gauss-Newton incremental scheme is implemented to retrieve displacements $\underline{u}^0$ and $\underline{u}^1$ associated with each problem that respectively deals with image I^0 or I^1. Since the resolution is identical in both cases, the general case of displacement $\underline{u}$ associated with image I is presented. Denoting by $\mathbf{u}^{(\mathsf{it})}$ the vector collecting the dof values $(u_i)_{1\leq i\leq n_{dof}}$ at increment "it", and from an initial guess $\mathbf{u}^{(0)}$, the matrix form of the iterative problem writes as follows

$$\mathbf{u}^{(\mathsf{it}+1)} = \mathbf{u}^{(\mathsf{it})} + \boldsymbol{\delta}\mathbf{u}, \text{ with } \mathbf{M}^{(\mathsf{it})} \times \boldsymbol{\delta}\mathbf{u} = \mathbf{b}^{(\mathsf{it})}(I), \tag{5}$$

where

$$[\mathbf{M}^{(\mathsf{it})}]_{ij} = \int_{\underline{x}\in\omega_{\mathsf{zp}}} \underline{\varphi}_i(\underline{x})\cdot\underline{\nabla}\mathcal{I}\left(\underline{x} + \sum_{k=1}^{n_{dof}} u_k\underline{\varphi}_k(\underline{x})\right)\times\underline{\varphi}_j(\underline{x})\cdot\underline{\nabla}\mathcal{I}\left(\underline{x} + \sum_{l=1}^{n_{dof}} u_l\underline{\varphi}_l(\underline{x})\right)\mathrm{d}\underline{x}, \tag{6}$$

and

$$[\mathbf{b}^{(\mathsf{it})}(I)]_i = \int_{\underline{x}\in\omega_{\mathsf{zp}}} \underline{\varphi}_i(\underline{x})\cdot\underline{\nabla}\mathcal{I}\left(\underline{x} + \sum_{k=1}^{n_{dof}} u_k\underline{\varphi}_k(\underline{x})\right)\times\left(I(\underline{x}) - \mathcal{I}\left(\underline{x} + \sum_{l=1}^{n_{dof}} u_l\underline{\varphi}_l(\underline{x})\right)\right)\mathrm{d}\underline{x}. \tag{7}$$

The bracket notation used here is such that $[\mathbf{A}]_{ij}$ corresponds to the element of the i^{th} line and the j^{th} column of matrix $\mathbf{A}$. The interested reader can refer to [18, 28] for further details about the obtention of this matrix form in the case of classic DIC. The tangent operator $\mathbf{M}^{(\mathsf{it})}$ does not depend on any experimental data. It is thus expected to be less sensitive to impairment caused by experiments such as sensor noise for instance.

In what follows, tangent operator $\mathbf{M}^{(\mathsf{it})}$ is simplified as discussed in [18, 28]. Consequently, it does not rely anymore on incremental values and its computation is performed once and for all before processing the real images

I^0 and I^1. Thus

$$[\mathbf{M}]_{ij} = \int_{\underline{x}\in\omega_{\underline{x}_\mathsf{p}}} \underline{\varphi}_i(\underline{x}) \cdot \underline{\nabla}\mathcal{I}(\underline{x}) \times \underline{\varphi}_j(\underline{x}) \cdot \underline{\nabla}\mathcal{I}(\underline{x}) \mathrm{d}\underline{x}. \tag{8}$$

In practice, quantities $\mathbf{M}$ and $\mathbf{b}$ are computed by using closed-form expressions obtained with Mathematica®, by considering first-order subset shape functions.

The proposed scheme is used for determining displacements $\underline{u}^0$ and $\underline{u}^1$ from images I^0 and I^1 respectively. The calculation of the displacement $\underline{u}$ that differentiates images I^0 and I^1 from the knowledge of $\underline{u}^0$ and $\underline{u}^1$, *cf* Equation (3), is performed with a fixed-point algorithm. In other words, from an initial guess $\underline{u}^{(0)}$, one has

$$\forall \underline{\mathsf{x}}_\mathsf{p} \in \mathrm{RoI}, \quad \underline{u}^{(\mathrm{it}+1)}(\underline{\mathsf{x}}_\mathsf{p}) = \underline{u}^0(\underline{\mathsf{x}}_\mathsf{p}) - \underline{u}^1\left(\underline{\mathsf{x}}_\mathsf{p} + \underline{u}^{(\mathrm{it})}(\underline{\mathsf{x}}_\mathsf{p})\right). \tag{9}$$

The iterative scheme is stopped when the difference between two successive increments is smaller than the usual measurement resolution of DIC, *i.e.* 10^{-3} [px]. In practice, since displacement features small gradients, the proposed procedure reaches convergence in a few iterations (less than 10). Moreover, the computation cost is rather low because it is reduced to calculation of the interpolation of $\underline{u}^1$ at non-integer positions. Finally, contrary to interpolation called in usual DIC procedures which concerns images, thus data featuring high gradients, interpolation is applied here to displacement fields, that corresponds to smooth data. The bias introduced here is therefore expected to be lower.

2.2 Principle of Virtual DIC - Practical case of optimal patterns

With the objective of obtaining measurements featuring the best possible metrological performance, the proposed method is illustrated with the pattern that appears to be optimal, namely the checkerboard, for which $\mathcal{I}$ reads as

follows:

$$\mathcal{I}(\underline{x}) = \mathcal{I}_{av} + \frac{\mathcal{I}_r}{2} \cos\left(\underline{x} \cdot \underline{k}\right) \cos\left(\underline{x} \cdot \underline{k}^{\perp}\right), \tag{10}$$

where $\mathcal{I}_{av}$ corresponds to the average gray level value of the virtual image, $\mathcal{I}_r$ to its dynamic range, and $(\underline{k}, \underline{k}^{\perp})$ are the wave vectors of the pattern. Considering a checkerboard made of white or black squares of width a [px], consequently of pitch $p = 2a$ [px], rotated by an angle α with respect to the reference system $(\underline{e}_1, \underline{e}_2)$, one has $\underline{k} = \frac{2\pi}{p}(\cos(\alpha)\underline{e}_1 + \sin(\alpha)\underline{e}_2)$. $\underline{k}^{\perp}$ corresponds to vector $\underline{k}$ rotated by $\pi/2$. In practice, the checkerboard is rotated to avoid aliasing [47]. Figure 3 illustrates the notation, where $\mathcal{I}_{av} = 125$ [GV], $\mathcal{I}_r = 125 \times 70\%$ [GV], $a = 4.5$ [px] and $\alpha = 10°$, where [GV] stands for "gray value". In practice checkerboard squares are poorly encoded by camera sensors, typically with about 3 pixels, as recommended by Reu [48]. As illustrated in Figure 3b, this low discretization smooths the edge of the squares and justifies the use of cosine functions for modelling the checkerboard images. Moreover, lenses are often characterized by their Point Spread Function that convolves light and thus also smooths image gradient. A closed-form expression that corresponds better to the acquired image might exist. Nevertheless, the compromise chosen here is to keep it as simple as possible for reducing computer costs.

Working with a periodic pattern is a drawback when classic approaches of Local DIC are used. Indeed, Local DIC retrieves local displacement that leads to the best matching, over small zones, between the deformed image and the reference image. At the subset scale, a periodic pattern causes the solution to converge to a local minimum. Nevertheless, the checkerboard texture appears to be optimal when considering sensor noise propagation to DIC output [37, 39, 40] or when considering PIB [29, 30]. This motivates the use of checkerboard for DIC. Some researchers introduced tricks for limiting the risk that DIC traps in local minima [37, 42, 43]. Generally, such approaches break pattern periodicity or introduce local changes of contrast. This consequently decreases the metrological performance obtained with these depleted checkerboards. The Virtual DIC approach proposes to work with a simple checkerboard pattern,

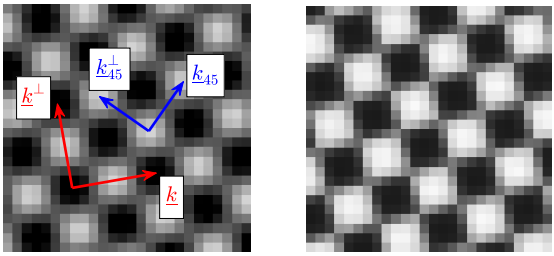

(a) (b)

Fig. 3: Closeup view of a virtual image modelling a checkerboard (a), and of a real checkerboard (b). The checkerboard of the virtual image has a pitch of $p = 2a = 2 \times 4.5$ [px]. It makes an angle of $\alpha = 10°$ with the border of the image. Despite the virtual image coming from a closed-form expression, only a poor discretized version is illustrated here to emphasize its resemblance with real checkerboard images.

the contrast and gradient distribution of which ensure optimal metrological performances.

The periodicity issue encountered by usual versions of DIC is circumvent with the proposed Virtual DIC. Virtual DIC is initialized, on purpose, with a null displacement field. Consequently, the retrieved displacement is always lower than the pitch of the pattern since a local solution exists. In the case of checkerboard patterns, the repetition of black and white squares along their diagonal reveals a pattern of pitch $\sqrt{2}a < 2a$. The wave lengths of this smallest periodicity are denoted here by $\underline{k}_{45}$ and $\underline{k}_{45}^{\perp}$. They are illustrated in Figure 3a. They define the reference system of the smallest pattern periodicity $(\underline{e}, \underline{e}^{\perp})$:

$$\underline{k}_{45} = \sqrt{2}a\ \underline{e} \text{ and } \underline{k}_{45}^{\perp} = \sqrt{2}a\ \underline{e}^{\perp}. \tag{11}$$

Considering an image I, Virtual DIC retrieves thus at every pixel position $\underline{\mathsf{x}}_{\mathsf{p}}$ displacement $\underline{u}(\underline{\mathsf{x}}_{\mathsf{p}})$, whose components in the basis $(\underline{e}, \underline{e}^{\perp})$ belong to $]-\sqrt{2}a, \sqrt{2}a]$. The obtained displacement is thus wrapped: when one of its components reaches one bound of its interval, its value jumps to the other extrema

of the interval. This occurs in space but also in time and the displacements fields needs to be unwrapped.

Spatial unwrapping

Spatially wrapped displacement is unwrapped here with a dedicated algorithm [49, 50]. It is worth noting that such a procedure is routinely applied in optics for instance, when dealing with phase unwrapping. An illustration is presented in Figure 4. It shows the displacement retrieved when Virtual DIC is applied on synthetic images generated with the speckle generator proposed in [51], which has been extended to checkerboard images. This synthetic checkerboard features squares of width $a = \pi$ [px] and makes an angle of 10° with direction $\underline{e}_1$. This width was chosen to avoid any singularity in the image generation. Note that other irrational number values close to 3 could also be used instead. The deformed image mimics here a homogeneous ε_{11} strain field of -5%. In other words, the corresponding displacement is affine and only along direction $\underline{e}_1$. The displacement field retrieved by Virtual DIC is shown in Figures 4a & 4c in the $(\underline{e}, \underline{e}^{\perp})$ basis. Jumps of amplitude equal to the pitch of the pattern are clearly visible. They are corrected by applying an unwrapping algorithm, see Figures 4b & 4d or the horizontal cross sections shown in Figures 4c & 4f. Unwrapping more complex displacement fields is illustrated later on this paper.

Note finally that displacement maps provided by classic DIC would also be wrapped, but unwrapping would be problematical in this case, the value of the pitch slightly spatially changing for real markings engraved for instance with the technique described in [35]. This would thus lead to spurious slight "jumps" in such displacement maps.

Temporal unwrapping

Wrapping discussed above also occurs temporally. Indeed, when applied to image I, Virtual DIC retrieves displacement field *modulo* pitch. Spatial

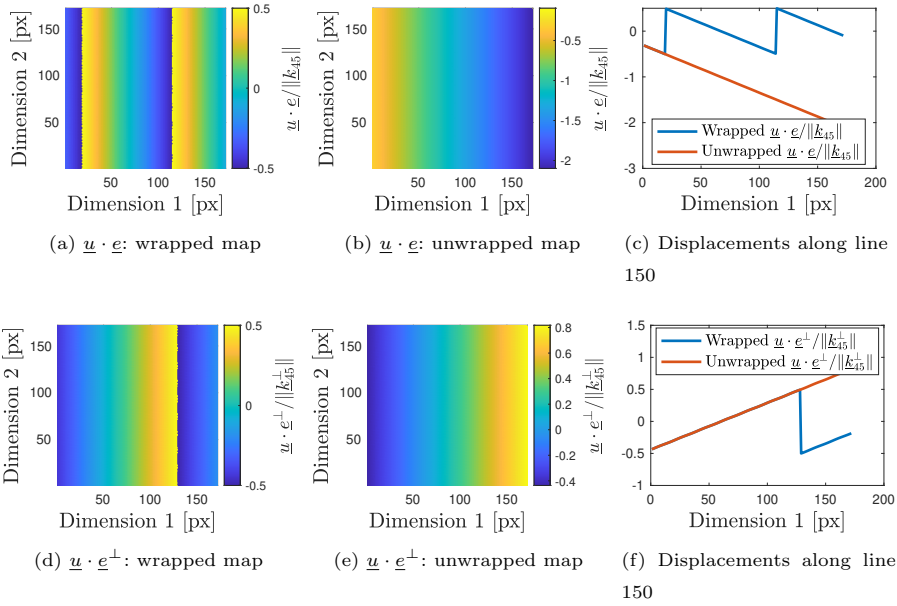

(a) $\underline{u} \cdot \underline{e}$: wrapped map (b) $\underline{u} \cdot \underline{e}$: unwrapped map (c) Displacements along line 150

(d) $\underline{u} \cdot \underline{e}^{\perp}$: wrapped map (e) $\underline{u} \cdot \underline{e}^{\perp}$: unwrapped map (f) Displacements along line 150

Fig. 4: Virtual DIC applied to a synthetically deformed image. The ground-truth deformation is a homogeneous ε_{11} strain field of -5%. The wrapped displacement retrieved by Virtual DIC is projected on the basis $(\underline{e}, \underline{e}^{\perp})$ of the smallest pattern periodicity and divided by the corresponding pitch, *i.e.* $\sqrt{2}a$. The quantities lie thus in $]-0.5, 0.5]$, as illustrated in Figures (a) and (d), and in the horizontal cross sections shown in Figures (c) and (f) in blue. Unwrapping the maps correct the jumps, as illustrated in Figures (b) and (e), and in the new horizontal cross sections shown in Figures (c) and (f) in red.

unwrapping corrects the spatial jumps, but temporal jumps shall also be investigated. Indeed, a multiple of the pitch is potentially added to the results obtained after spatial unwrapping, depending on the location of the origin of displacement chosen for this spatial unwrapping. As previously detailed, the sought displacement field $\underline{u}$ is determined from the calculation of displacements $\underline{u}^0$ and $\underline{u}^1$ associated with images I^0 and I^1 respectively, by solving the problem given by Equation (3)&(4). After spatial unwrapping, Equation (3) is modified to take any possible temporal wrapping into account. This is done

by introducing two integers, denoted here by Δ and $\Delta^{\perp}$, such that:

$$\forall \underline{\mathrm{x}}_{\mathrm{p}} \in \mathrm{RoI}, \quad \underline{u}(\underline{\mathrm{x}}_{\mathrm{p}}) = \underline{u}^{0}(\underline{\mathrm{x}}_{\mathrm{p}}) - \underline{u}^{1}\left(\underline{\mathrm{x}}_{\mathrm{p}} + \underline{u}(\underline{\mathrm{x}}_{\mathrm{p}})\right) + \Delta \underline{k}_{45} + \Delta^{\perp} \underline{k}_{45}^{\perp}. \tag{12}$$

In practice, Δ and $\Delta^{\perp}$ are easily determined by measuring displacement $\underline{u}$ at an arbitrary point denoted by $\underline{\mathrm{x}}_{\mathrm{p}}^{d}$. Point $\underline{\mathrm{x}}_{\mathrm{p}}^{d}$ often corresponds to a marking defect, which is simply defined in I^{0} and retrieved in I^{1}. Marking defects usually feature specific signatures and are thus easily recognizable from one image to another. If pattern depositing reaches outstanding performance and deposited checkerboard appears perfect, deliberately introducing a defect appears as a simple and effective solution.

Displacement $\underline{u}(\underline{\mathrm{x}}_{\mathrm{p}}^{d})$ is therefore easily measured at a pixel resolution, and the projection of Equation (12) to $\underline{e}$ and $\underline{e}^{\perp}$ gives:

$$\begin{cases} \Delta = \dfrac{\left(\underline{u}(\underline{\mathrm{x}}_{\mathrm{p}}^{d}) - \underline{u}^{0}(\underline{\mathrm{x}}_{\mathrm{p}}^{d}) + \underline{u}^{1}\left(\underline{\mathrm{x}}_{\mathrm{p}}^{d} + \underline{u}(\underline{\mathrm{x}}_{\mathrm{p}}^{d})\right)\right) \cdot \underline{e}}{\|\underline{k}_{45}\|} \\ \Delta^{\perp} = \dfrac{\left(\underline{u}(\underline{\mathrm{x}}_{\mathrm{p}}^{d}) - \underline{u}^{0}(\underline{\mathrm{x}}_{\mathrm{p}}^{d}) + \underline{u}^{1}\left(\underline{\mathrm{x}}_{\mathrm{p}}^{d} + \underline{u}(\underline{\mathrm{x}}_{\mathrm{p}}^{d})\right)\right) \cdot \underline{e}^{\perp}}{\|\underline{k}_{45}^{\perp}\|} \end{cases}. \tag{13}$$

To avoid any numerical issues, Δ and $\Delta^{\perp}$ are determined by rounding to the closest integer the right-hand side terms.

Optimal patterns, *i.e.* checkerboards, are periodic patterns. This periodicity causes the solution given by regular versions of DIC to be entrapped in local minima. Spatial and temporal unwrapping allows Virtual DIC to circumvent this issue. Similar unwrapping procedure is already employed when periodic patterns are processed by spectral techniques such as the Localized Spectrum Analysis (LSA) [41]. Indeed, the latter solves Equation (4) in the Fourier domain and retrieves the phase modulation that deforms this periodic pattern. However, phases are computed modulo 2π. They are therefore spatially and temporally wrapped, similarly to the displacement with Virtual DIC.

A first advantage of Virtual DIC is to correctly process checkerboard patterns. A second one is to rely on the DIC framework, which is quite popular in the experimental mechanics community. This makes it possible to consider

its extension to stereo measurements for instance or to many other extensions of 2D DIC in future studies such as stereo DIC. On the contrary, such extensions/improvements are not currently available for LSA.

3 Assessment of metrological performances

The comparison of results obtained with checkerboards and classic random speckles has been detailed in some previous papers [37, 39]. The main conclusion is that the checkerboard pattern leads to the best metrological performance. Application with DIC was thus limited because of the pattern periodicity which drives DIC to local minima. Thanks to Virtual DIC that includes a virtual image of a perfectly mastered pitch, unwrapping is possible and its application allows the checkerboard process for optimized metrological performance. The definition of the parameters that characterize the metrological performance of a full-field measurement, *i.e.* the measurement resolution, the bias, and the spatial resolution, is detailed in the appendix and thoroughly investigated in [27, 32]. Only checkerboard patterns are therefore considered in the following text.

3.1 Interpolation bias

First, interpolation bias is investigated. This bias is the fact that for usual DIC, the formulation scheme (backward, forward or mixed) involves evaluation at subpixel positions of at least one image. This bias is often illustrated by using a set of synthetic images, which mimic subpixel translations. Here, 10 images of size 128×128 pixels have been generated with the generalization to checkerboard images of the speckle generator proposed in [51]. The generator was set to mimic the acquisition of a checkerboard made of squares of side $a = 3$ [px] and with an angle of 10° with direction $\underline{e}_1$. The contrast was set to 33% of an 8-bit dynamic range. The first image defines the reference state I^0. A translation along direction $\underline{e}_1$ of $k/10$ [px], with $k \in \{1, ..., 9\}$ was then used for generating 9 current images $(I^k)_{1 \leq k \leq 9}$. DIC and Virtual DIC were applied on these

9 pairs of images. Because these displacements were smaller than the checkerboard pitch, DIC retrieved the correct displacement. For both approaches, the subset size was set to $2 \times h + 1 = 21$ [px] and subset shape functions are of first order. Two DIC interpolation schemes were studied: the bi-cubic and the bi-spline schemes. Finally, the parameters $(\mathcal{I}_{av}, \mathcal{I}_r, \underline{k}, \underline{k}^{\perp})$ of the closed-form expression that defines the virtual image, see Equation (10), were computed from the reference image I^0. Although ground-truth parameters are known in this particular case of synthetic images, using the identified parameters from a discrete image is more representative of real cases. The dynamic range of I^0 directly gives $\mathcal{I}_r = 70$ [GV] and its averaged value $\mathcal{I}_{av} = 128$ [GV]. The localisation of the highest peak in the discrete Fourier transform of the reference image I^0 is used for computing the pitch $p = \sqrt{2} \times 2.97$ [px] and the angle $\alpha = 10.87°$ that define the wave length parameters $\underline{k}$ and $\underline{k}^{\perp}$.

Figure 5 displays the average of the $\underline{e}_1$-component of the displacement error when DIC and Virtual DIC are applied to each image pair. The usual S-shaped curve of interpolation bias is retrieved for the classic subset-based DIC implementations. Spline interpolation attenuates this bias. As expected, Virtual DIC gives almost no interpolation bias. The maximum of the error reaches 4.83×10^{-4} [px], value which is below the usual measurement resolution of full-field measurement techniques. As a general remark, all techniques retrieve the displacement of 0.5 [px] without bias.

3.2 Spatial resolution and bias

A commonly accepted assessment of spatial resolution relies on the "star" images of the DIC Challenge [32]. It consists of studying a pair of images, which are differentiated by a specific displacement. This displacement, of direction $\underline{e}_2$ only, is a sine function of 0.5 [px] amplitude, whose period linearly evolves from 10 [px] to 140 [px]. Full-field measurement techniques act as low-pass filtering approaches. Applying them on the star images highlights their corresponding cut-off property, which is used to define their spatial resolution.

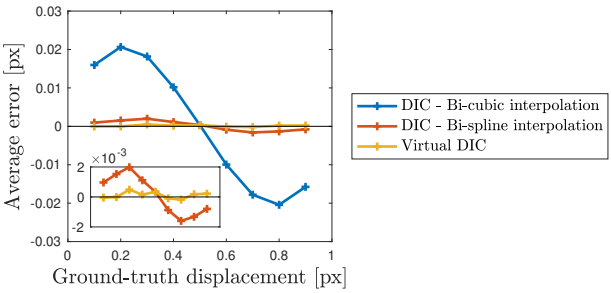

Fig. 5: The usual S-shaped curve corresponds to the interpolation bias. The inset shows results for the DIC with bi-spline interpolation and Virtual DIC only. DIC and Virtual DIC are applied to synthetic images mimicking sub-pixel translations. Average measurement errors in the direction of the movement are computed for each translation. Both bi-cubic and spline interpolations have been implemented for DIC measurements. As expected, Virtual DIC is not affected by interpolation bias.

Synthetic images are generated for this purpose. They consist here of checkerboard images with the following parameters: $a = 3$ [px], $\alpha = 10°$ and the contrast is set to two thirds of an 8-bit dynamic range. Noise is also added to the images. The associated parameters correspond to the those of [32].

Similarly to the previous section, the closed-form expression of the virtual image used in Virtual DIC relies on parameters identified from the reference discretized image: $p = \sqrt{2} \times 2.99$ [px], $\alpha = 10.00°$, $\mathcal{I}_r = 168$ [GV], and $\mathcal{I}_{av} = 128$ [GV]. These identified parameters are closest to the ones used for image generation described in the preceding section (2.99 instead of 2.97 in Section 3.1). The reference image contains indeed more pixels (501×2000 pixels versus 128×128 pixels). Consequently, its spectral representation is also richer and the peak location is more accurately encoded and identified.

DIC and Virtual DIC were applied on these "star" images, with a subset size set by $2 \times h + 1 = 21$ [px] and first-order subset shape functions. DIC relies on spline interpolation. Again, since displacement remains smaller than the pattern pitch, classic DIC retrieves the correct displacement field.

Figure 6 illustrates the $\underline{e}_2$-component of the displacement obtained with both techniques. Figure 6a shows the displacement map obtained with Virtual DIC. The low-pass filtering effect is clearly observable. Indeed, the high frequencies on the left-hand side of the map are not retrieved by the measurement technique. Results obtained along the midline displayed in red in Figure 6a are shown Figure 6b. Both techniques, *i.e.* DIC and Virtual DIC, behave similarly. The retrieved displacement is close to the black dashed line, which is the convolution of the ground-truth displacement with a Savitzky-Golay kernel of the first order and of size $2 \times h + 1$, as theoretically expected [10, 29, 52]. Results are close to those produced by the Savitzky-Golay convolution because the PIB is low when checkerboards are used [37, 39, 40]. The insert in Figure 6b is a closeup view of the results, for sine displacement of periods ranging from 38 [px] to 45 [px]. The displacement obtained with Virtual DIC appears to be slightly lower but it is also smoother. It is therefore less sensitive to image noise or to image texture. Such results are possible because the interpolation bias discussed in the preceding section is not involved when studying the midline of the star image. Indeed, ground-truth displacement reaches 0.5 [px] along this line. When such images, first proposed in [53], have been extended to the study of the metrological performance of the DIC technique [52], this magnitude of 0.5 [px] was deliberately chosen to separate the sources of bias. For the displacement of 0.5 [px], there is indeed no interpolation bias (see Figure 5).

To conclude this section, spatial resolution and bias are very similar for DIC and Virtual DIC. It is worth noting that this academic case meets the assumptions under which classic DIC works correctly: displacements are smaller than pattern pitch and interpolation bias is null. The next section investigates noise propagation in DIC and Virtual DIC in a more realistic case.

3.3 Illustration

In this section, bias and measurement resolution are studied through an academic synthetic example that mimics a real test. The specific case of

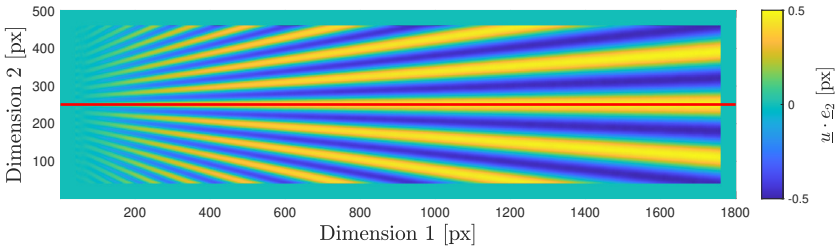

(a)

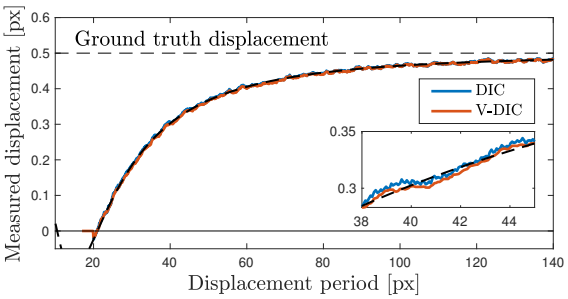

(b)

Fig. 6: Applying DIC and Virtual DIC to the "star" images of the DIC Challenge [32]. (a) Map of the $\underline{e}_2$-component of the displacement obtained with Virtual DIC. Note the low-pass filtering effect of DIC: high frequencies on the left-hand side of the map are attenuated. (b) Displacements along the midline, which is displayed in red in (a). The abscissa here directly gives the period of sine wave that defines ground-truth displacement. DIC and Virtual DIC perform similarly.

displacement surrounding a hole of an infinite plate subjected to tension is investigated here. An illustration of the plate is given in Figure 7a. Ground-truth displacement $\underline{u}_{GT}$ is defined by

$$\underline{u}_{GT}(r,\theta) = u^0_{GT}\left[\left((1+\nu)\left(\frac{r_h^2}{r}+(r-\frac{r_h^4}{r^3})\cos(2\theta)\right)+(1-\nu)r+\frac{4r_h^2}{r}\cos(2\theta)\right)\underline{e}_r - \left((1+\nu)\left(1+\frac{r_h^4}{r^4}\right)r+(1-\nu)\frac{2r_h^2}{r}\sin(2\theta)\right)\underline{e}_\theta\right], \quad (14)$$

where u^0_{GT} relies on Young's modulus E of the constitutive material of the plate, and on the prescribed external pressure σ_0: $u^0_{GT} = \sigma_0/2E$. ν is Poisson's

ratio, and r_h the radius of the hole. (r, θ) are the polar coordinates of any point of the plate with respect to the center of the hole expressed in the polar coordinate system $(\underline{e}_r, \underline{e}_\theta)$. The latter corresponds to $(\underline{e}_1, \underline{e}_2)$ when $\theta = 0$.

The images generated in this case are 512×512 pixels in size, with the hole at the center in the reference state, $\nu = 0.3$, $r = 50$ [px], and u^0_{GT} were set such that the maximum displacement in the plate reaches 5 [px]. The pattern is a checkerboard of squares of side 3 [px], with an angle of 10° and a contrast of 40% of the 8−bit dynamic range. Both the DIC and the Virtual DIC implementations rely on subsets of a size set by $2 \times h + 1 = 21$ [px] and first-order subset shape functions. Spline interpolation is used for DIC. The closed-form expression of the virtual image used in Virtual DIC relies on parameters identified from the reference discretized image: $p = \sqrt{2} \times 2.99$ [px], $\alpha = 9.74°$, $\mathcal{I}_r = 198$ [GV], and $\mathcal{I}_{av} = 90$ [GV]. Because displacements are in some zones greater than the pattern pitch, DIC is initialized with the displacement retrieved by Virtual DIC.

Displacements retrieved with Virtual DIC are displayed in Figure 7. Virtual DIC first computes the two displacements that distinguish the virtual image from both the experimental images. The wrapped displacements are shown in Figure 7b, 7c, 7e & 7f. Once unwrapped, these displacements feed Equation (9), which eventually gives the displacement that really deforms the current image with respect to the reference image. Both components of the retrieved displacement are illustrated in Figure 7d & 7g.

Bias

We consider noiseless images here. Virtual DIC and then DIC are applied on a pair of images. Since the present case study relies on synthetic images, ground-truth displacement is known and used for comparison purposes. DIC and Virtual DIC outputs are thus compared to the best possible measurement, *i.e.* to the ground-truth solution convolved with a Savitzky-Golay kernel denoted by w_{SG} of width $2 \times h + 1$ and of first-order. A vectorial error is

introduced and its norm is defined by:

$$\|\underline{u} - \underline{u}_{GT} * w_{SG}\| = \sqrt{\left(u_x - u_{GT,x} * w_{SG}\right)^2 + \left(u_y - u_{GT,y} * w_{SG}\right)^2}, \quad (15)$$

where "$*$" denotes the convolution product. This error is illustrated in Figure 8.

Several remarks can be drawn from these results:

- The mean value of the error of the results obtained with Virtual DIC is slightly smaller than with usual DIC. In this case, the improvement is about 12%. The fact that Virtual DIC output is not affected by the interpolation scheme probably explains this result.
- The dispersions of the errors are of the same order of magnitude for the two DIC techniques. The errors of Virtual DIC are slightly smaller (6%).
- Spatial correlation is observable in both error maps, see Figure 8a for DIC and Figure 8b for Virtual DIC. Interestingly, the spatial correlation of the error appears to be smaller for Virtual DIC.

Measurement error

The measurement resolution of DIC and Virtual DIC has also been investigated in this case. For this purpose, 100 pairs of images were generated. 100 pairs of different copies of a heteroscedastic noise satisfying the properties proposed in [32] were added to the noiseless pair of images used in Section 3.3 in order to generate the noisy set of images. Virtual DIC and DIC were applied in turn to each pair of images. 100 maps of displacement $(\underline{u}_i)_{1\leq i\leq 100}$ are thus retrieved with each measurement technique. For each approach, the standard deviation characterizing the dispersion of the outputs was computed as follows, $\forall \underline{\mathsf{x}}_\mathsf{p} \in \text{RoI}$, $\forall \ell \in \{1,2\}$:

$$std\left(\underline{u}(\underline{\mathsf{x}}_\mathsf{p}) \cdot \underline{e}_\ell\right) = \sqrt{\frac{1}{99}\sum_{i=1}^{100}\left(\underline{u}_i(\underline{\mathsf{x}}_\mathsf{p}) \cdot \underline{e}_\ell - \langle \underline{u}_i(\underline{\mathsf{x}}_\mathsf{p}) \cdot \underline{e}_\ell \rangle_{1\leq i\leq 100}\right)^2}, \quad (16)$$

with $\langle\cdot\rangle$ the averaging operator: $\langle a_i(\underline{\mathtt{x}}_\mathtt{p})\rangle_{1\leq i\leq N} = \frac{1}{N}\sum_{i=1}^{N} a_i(\underline{\mathtt{x}}_\mathtt{p})$. For each method, the spatial distribution of the standard deviation observed for each component of the displacement is shown in Figure 9. Contrary to the bias, the spatial dispersion of the measurement resolution of both techniques is identical. The same data are also presented with histograms to help characterize their dispersion. The conclusion remains the same: dispersion is similar from one technique to another.

A commonly used method for enhancing measurement resolution consists in taking a stack of images of the reference state. Theses images are then averaged to form a reference image where the noise is considered to be minimized. This image then serves as the reference image with DIC. However, tiny movements between camera and specimen may occur while taking the stack of images. In this case, the consequence is that the mean image is a biased estimator of the noise-free image. This hurdle can be circumvented with Virtual DIC by averaging the virtual displacements obtained with the numerous images that would correspond to the reference state instead of averaging the image themselves. The influence of such parasitic movements have been studied in [22] . A procedure has been proposed for removing them from the images but this technique only works in the case of periodic patterns.

4 Challenging real case

In this last section, Virtual DIC is applied to a real and challenging case. We considered a notched aluminum plate of dimensions 200 [mm] $\times$40 [mm] $\times$ 2 [mm]. It was subjected to tensile loading. A notch of dimensions 20 [mm] $\times$1 [mm] was machined before the test at the middle of the longest direction of the specimen, which corresponds to the direction of the load. A checkerboard pattern was deposited onto the specimen surface using the procedure proposed in [54]. The imaged surface is shown in Figure 10. Images were acquired with a PCO 2000 camera with a 4Mpixel CCD sensor equipped with a 100 [mm] Tokina lens.

This case is challenging because:

- The pattern is not perfect anymore, as it was the case with the synthetic images studied previously. Among other things, local pitch variations are observed. In addition, the light is not homogeneous. See the fluctuations in the pattern amplitude of the gray level distribution along the green line plotted in Figure 10a, and illustrated in Figure 10b. Marking is also missing at some points, see two defects in the red square plotted in Figure 10c.
- Fracture occurs at the tip of the notch and propagates. The pattern considerably changes in this zone, as illustrated by the blue arrow in the deformed image shown in Figure 10d. This local degradation of the marking can potentially jeopardize correct determination of displacement in this zone;
- The current image corresponds to a high value of the load. The strain and the displacement components are significant. The latter are expected to be greater than the pattern pitch in some zones;
- Sharp strain localization occurs at the crack tip.

Despite our in-house DIC code features metrological performance, which is similar to those of usual DIC commercial codes [32], it does not accept seed point and cannot deal with checkerboard pattern except if well initialized. When initialized with the displacement field found with the Virtual DIC solution and when considering a region of interest away from the crack tip and lips, the result provided by our in-house DIC code is similar to that obtained with Virtual DIC in the same zone. However, our DIC code cannot correctly deal with images containing a crack, thus further comparison is not possible.

The parameters of the virtual image are as follows: $p = \sqrt{2} \times 3.00$ [px], $\alpha = 1.00°$, $\mathcal{I}_r = 240$ [GV], and $\mathcal{I}_{av} = 130$ [GV]. Figure 11 presents the $\underline{u}^0$ and $\underline{u}^1$ displacement maps retrieved by Virtual DIC. The first column, *i.e.* Figure 11a & 11d, shows the wrapped displacement $\underline{u}^0$ retrieved along the directions $(\underline{e}, \underline{e}^\perp)$ from the reference image to the virtual image. The second

column, *i.e.* Figure 11b & 11e, depicts both components of the wrapped displacement $\underline{u}^1$ retrieved between the deformed image and the virtual image. These maps allow for a few observations:

- Numerous fringes are observable in the reference state, see Figures 11a & 11d. This is due to the fact that the pitch of the virtual image is not rigorously equal to the real pitch of the reference image;
- Considering the current state, *i.e.* Figures 11b & 11e, the right-hand part of the specimen features more fringes than its left-hand side. During the tensile test, the moving grip was on the right-hand side of the specimen. Once the fracture process started, specimen stiffness drastically decreased, and the specimen plastically rotated around the crack tip. Consequently, the right-hand side of the specimen experienced greater rotation, which explains the numerous fringes in the $\underline{u}_1$ maps;
- Closeup views of the wrapped value of displacement $\underline{u}^0$ are shown in Figures 11c & 11f. They correspond to the red square in Figure 10a, which is enlarged in Figure 10c. In the reference state, local defects are observable. Their location corresponds to the red crosses of Figure 11c & 11f. These closeup views reveal that these pattern defects do not impair the wrapped displacement fields returned by Virtual DIC.

Unwrapping both the $\underline{u}^0$ and $\underline{u}^1$ maps and solving Equation (9) provide the displacement field between the reference and the current images. Its $\underline{e}_1$- and $\underline{e}_2$-components are depicted in Figure 12. It is worth noting that the unwrapping algorithm correctly unwraps the wrapped displacement fields. The range of the displacement, which is about 50 [px], is much greater than the pattern pitch (a is equal here to 3 [px]). Virtual DIC can thus process the optimal DIC pattern, *i.e.* the checkerboard, without being trapped in any local minima. Despite the presence of the singularity caused by the crack and high pattern changes, the displacement field close to the crack tip remains quite smooth, without any local disturbance.

5 Conclusion

This paper introduces a novel version of DIC named Virtual DIC. Its backbone is based on the closed-form expression of the image texture called virtual image. The real images are the discretized versions of the virtual pattern because the latter is deposited on the surface under study. The determination of the virtual displacements differentiating the virtual image from the real images allows the calculation of the real displacement from one real image to the other. Because the information carrier is mastered, the benefits of this Virtual DIC are: (i) *it reduces random errors*- The virtual image is used to build up the DIC solver. The DIC operators rely on the closed-form expression of the virtual image instead of on real (thus noisy) images of this pattern. This reduces the impact of acquisition noise in the final results; (ii) *it reduces systematic errors*- Real discretized images are not interpolated because the DIC solver refers to the closed-form expression of the virtual image. This leads to an interpolation-free DIC approach and thus overcomes one of the limitations of usual DIC versions; (iii) *it improves DIC metrological performance*- Virtual DIC correctly processes checkerboard patterns. Periodicity issue of usual version of DIC is circumvent. The checkerboard pattern is indeed the optimal pattern since it minimizes sensor noise propagation and Pattern-Induced Bias.

Further studies will consider extensions of Virtual DIC to Global DIC and stereo DIC approaches.

6 Acknowledgements

The authors acknowledge support from the ANR Grant ANR-18-CE08-0028-01. This work was also sponsored by the French government research program "Investissements d'Avenir" through the IDEX-ISITE initiative 16-IDEX-0001 (CAP 20-25), and from the AURA regional council.

Ethics declarations/Conflict of Interest

The authors declare that they have no conflict of interest.

References

[1] Sutton, M.A., Mingqi, C., Peters, W.H., Chao, Y.J., McNeill, S.R.: Application of an optimized digital correlation method to planar deformation analysis. Image and Vision Computing **4**(3), 143–150 (1986). https://doi.org/10.1016/0262-8856(86)90057-0

[2] Garcia, D.: Mesure de formes et de champs de déplacements tridimensionnels par stéréo-corrélation d'images. PhD thesis, Institut National Polytechnique de Toulouse (2001)

[3] Wang, Y., Lava, P., Coppieters, S., Houtte, P.V., Debruyne, D.: Application of a multi-camera stereo dic set-up to assess strain fields in an erichsen test: Methodology and validation. Strain **49**(2), 190–198 (2013). https://doi.org/10.1111/str.12027

[4] Dufour, J.-E., Hild, F., Roux, S.: Shape, displacement and mechanical properties from isogeometric multiview stereocorrelation. The Journal of Strain Analysis for Engineering Design **50**(7), 470–487 (2015). https://doi.org/10.1177/0309324715592530

[5] Passieux, J.-C., Bugarin, F., David, C., Périé, J.-N., Robert, L.: Multiscale displacement field measurement using digital image correlation: Application to the identification of elastic properties. Experimental Mechanics **55**(1), 121–137 (2015). https://doi.org/10.1007/s11340-014-9872-4

[6] Bay, B.K., Smith, T.S., Fyhrie, D.P., Saad, M.: Digital volume correlation: Three-dimensional strain mapping using x-ray tomography. Experimental Mechanics **39**(3), 217–226 (1999). https://doi.org/10.1007/BF02323555

[7] Jailin, C., Buljac, A., Bouterf, A., Hild, F., Roux, S.: Fast 4D tensile test monitored via X-CT: Single projection based Digital Volume Correlation dedicated to slender samples. Journal of Strain Analysis for Engineering Design (2018)

[8] Lucas, B.D., Kanade, T.: An iterative image registration technique with an application to stereo vision. In: Proceedings of the 7th International Joint Conference on Artificial Intelligence - Volume 2. IJCAI'81, pp. 674–679. Morgan Kaufmann Publishers Inc., San Francisco, CA, USA (1981). http://dl.acm.org/citation.cfm?id=1623264.1623280

[9] Baker, S., Matthews, I.: Lucas-kanade 20 years on: A unifying framework. International Journal of Computer Vision **56**(3), 221–255 (2004). https://doi.org/10.1023/B:VISI.0000011205.11775.fd

[10] Schreier, H.W., Sutton, M.A.: Systematic errors in digital image correlation due to undermatched subset shape functions. Experimental Mechanics **42**(3), 303–310 (2002). https://doi.org/10.1007/BF02410987

[11] Wang, Y.Q., Sutton, M.A., Bruck, H.A., Schreier, H.W.: Quantitative error assessment in pattern matching: Effects of intensity pattern noise, interpolation, strain and image contrast on motion measurements. Strain **45**(2), 160–178 (2009). https://doi.org/10.1111/j.1475-1305.2008.00592.x

[12] Wang, Y.Q., Sutton, M.A., Ke, X.D., Schreier, H.W., Reu, P.L., Miller, T.J.: On error assessment in stereo-based deformation measurements. Experimental Mechanics **51**(4), 405–422 (2011)

[13] Ke, X.D., Schreier, H.W., Sutton, M.A., Wang, Y.Q.: On error assessment in stereo-based deformation measurements. Experimental Mechanics **51**(4), 423–441 (2011)

[14] Pan, B., Yu, L., Wu, D., Tang, L.: Systematic errors in two-dimensional

digital image correlation due to lens distortion. Optics and Lasers in Engineering **51**(2), 140–147 (2013). https://doi.org/10.1016/j.optlaseng.2012.08.012

[15] Pan, B.: Bias error reduction of digital image correlation using gaussian pre-filtering. Optics and Lasers in Engineering **51**(10), 1161–1167 (2013). https://doi.org/10.1016/j.optlaseng.2013.04.009

[16] Pan, B., Yu, L., Wu, D.: High-accuracy 2d digital image correlation measurements with bilateral telecentric lenses: Error analysis and experimental verification. Experimental Mechanics **53**(9), 1719–1733 (2013). https://doi.org/10.1007/s11340-013-9774-x

[17] Pan, B., Xie, H., Wang, Z.: Equivalence of digital image correlation criteria for pattern matching. Appl. Opt. **49**(28), 5501–5509 (2010). https://doi.org/10.1364/AO.49.005501

[18] Neggers, J., Blaysat, B., Hoefnagels, J.P.M., Geers, M.G.D.: On image gradients in digital image correlation. International Journal for Numerical Methods in Engineering **105**(4), 243–260 (2016). https://doi.org/10.1002/nme.4971

[19] Wang, Y., Lava, P., Reu, P., Debruyne, D.: Theoretical analysis on the measurement errors of local 2d dic: Part i temporal and spatial uncertainty quantification of displacement measurements. Strain **52**(2), 110–128 (2016). https://doi.org/10.1111/str.12173

[20] Su, Y., Zhang, Q., Xu, X., Gao, Z.: Quality assessment of speckle patterns for dic by consideration of both systematic errors and random errors. Optics and Lasers in Engineering **86**, 132–142 (2016). https://doi.org/10.1016/j.optlaseng.2016.05.019

[21] Blaysat, B., Grédiac, M., Sur, F.: Effect of interpolation on noise propagation from images to DIC displacement maps. International Journal

for Numerical Methods in Engineering **108**(3), 213–232 (2016) https://arxiv.org/abs/hal-01255944. https://doi.org/10.1002/nme.5212

[22] Blaysat, B., Grédiac, M., Sur, F.: On the propagation of camera sensor noise to displacement maps obtained by DIC - an experimental study. Experimental Mechanics **56**(6), 919–944 (2016) https://arxiv.org/abs/hal-01269655. https://doi.org/10.1007/s11340-016-0130-9

[23] Rossi, M., Lava, P., Pierron, F., Debruyne, D., Sasso, M.: Effect of dic spatial resolution, noise and interpolation error on identification results with the VFM. Strain **51**(3), 206–222 (2015). https://doi.org/10.1111/str.12134

[24] Bomarito, G.F., Ruggles, T.J., Hochhalter, J.D., Cannon, A.H.: Investigation of Optimal Digital Image Correlation Patterns for Deformation Measurement. In: Sutton, M., Reu, P.L. (eds.) International Digital Imaging Correlation Society. Conference Proceedings of the Society for Experimental Mechanics Series. Springer, (2017). https://doi.org/10.1007/978-3-319-51439-0_5. $http://dx.doi.org/10.1007/978-3-319-51439-0_51$

[25] Lehoucq, R.B., Reu, P.L., Turner, D.Z.: The effect of the ill-posed problem on quantitative error assessment in digital image correlation. Experimental Mechanics (2017). https://doi.org/10.1007/s11340-017-0360-5

[26] Reu, P.L., Toussaint, E., Jones, E., Bruck, H.A., Iadicola, M., Balcaen, R., Turner, D.Z., Siebert, T., Lava, P., Simonsen, M.: Dic challenge: Developing images and guidelines for evaluating accuracy and resolution of 2d analyses. Experimental Mechanics **58**(7), 1067–1099 (2018). https://doi.org/10.1007/s11340-017-0349-0

[27] Blaysat, B., Neggers, J., Grédiac, M., Sur, F.: Towards criteria characterizing the metrological performance of full-field measurement techniques - Application to the comparison between local and global versions of DIC.

Experimental Mechanics **60**(3), 393–407 (2020) https://arxiv.org/abs/hal-02436541. https://doi.org/10.1007/s11340-019-00566-4

[28] Passieux, J.-C., Bouclier, R.: Classic and Inverse Compositional Gauss-Newton in Global DIC. International Journal for Numerical Methods in Engineering **119**(6), 453–468 (2019). https://doi.org/10.1002/nme.6057

[29] Sur, F., Blaysat, B., Grédiac, M.: On biases in displacement estimation for image registration, with a focus on Photomechanics. Journal of Mathematical Imaging and Vision **63**, 777–806 (2021)

[30] Fayad, S.S., Seidl, D.T., Reu, P.L.: Spatial dic errors due to pattern-induced bias and grey level discretization. Experimental Mechanics **60**(2), 249–263 (2020). https://doi.org/10.1007/s11340-019-00553-9

[31] Fouque, R., Bouclier, R., Passieux, J.-C., Périé, J.-N.: Fractal pattern for multiscale digital image correlation. Experimental Mechanics **61**(3), 483–497 (2021). https://doi.org/10.1007/s11340-020-00649-7

[32] Reu, P.L., Blaysat, B., Andó, E., Bhattacharya, K., Couture, C., Couty, V., Deb, D., Fayad, S.S., Iadicola, M.A., Jaminion, S., Klein, M., Landauer, A.K., Lava, P., Liu, M., Luan, L.K., Olufsen, S.N., Réthoré, J., Roubin, E., Seidl, D.T., Siebert, T., Stamati, O., Toussaint, E., Turner, D., Vemulapati, C.S.R., Weikert, T., Witz, J.F., Witzel, O., Yang, J.: DIC Challenge 2.0: Developing Images and Guidelines for Evaluating Accuracy and Resolution of 2D Analyses. Experimental Mechanics (2022). https://doi.org/10.1007/s11340-021-00806-6

[33] Jovani, T., Chanal, H., Blaysat, B., Grédiac, M.: Direct residual stress identification during machining. Journal of Manufacturing Processes **82**, 678-688 (2022). https://doi.org/10.1016/j.jmapro.2022.08.015

[34] Rouwane, A., Bouclier, R., Passieux, J.-C., Périé, J.-N.: Architecture-driven digital image correlation technique (ADDICT) for the measurement of sub-cellular kinematic fields in speckle-free cellular materials. International Journal of Solids and Structures **234-235**, 111223 (2022). https://doi.org/10.1016/j.ijsolstr.2021.111223

[35] Bouyra, Q., Blaysat, B., Chanal, H., Grédiac, M.: Using laser marking to engrave optimal patterns for in-plane displacement and strain measurement. Strain **58**(2), 12404 (2022). https://doi.org/10.1111/str.12404

[36] Bossuyt, S.: Optimized Patterns for Digital Image Correlation. In: Proceedings of the 2012 Annual Conference on Experimental and Applied Mechanics, vol. 3, pp. 239–248 (2013). http://dx.doi.org/10.1007/978-1-4614-4235-6_34

[37] Shi, Y., Blaysat, B., Chanal, H., Grédiac, M.: Designing Patterns for DIC with Poisson Image Editing. Experimental Mechanics **available online** (2022). https://doi.org/10.1007/s11340-022-00862-6

[38] Hao, Z., Chen, G., Ke, H., Deng, L., Liu, L.: Characterization of out-of-plane tensile stress–strain behavior for GFRP composite materials at elevated temperatures. Composite Structures **290**, 115477 (2022). https://doi.org/10.1016/j.compstruct.2022.115477

[39] Grédiac, M., Blaysat, B., Sur, F.: On the optimal pattern for displacement field measurement: random speckle and DIC, or checkerboard and LSA? Experimental Mechanics **60**, 509–534 (2019) https://arxiv.org/abs/hal-02462030. https://doi.org/10.1007/s11340-019-00579-z

[40] Bomarito, G.F., Hochhalter, J.D., Ruggles, T.J., Cannon, A.H.: Increasing accuracy and precision of digital image correlation through pattern optimization. Optics and Lasers in Engineering **91**, 73–85 (2017). https:

//doi.org/10.1016/j.optlaseng.2016.11.005

[41] Grédiac, M., Blaysat, B., Sur, F.: Extracting displacement and strain fields from checkerboard images with the localized spectrum analysis. Experimental Mechanics **59**(2), 207–218 (2019) https://arxiv.org/abs/hal-01926054. https://doi.org/10.1007/s11340-018-00439-2

[42] Bomarito, G.F., Hochhalter, J.D., Ruggles, T.J.: Development of optimal multiscale patterns for digital image correlation via local grayscale variation. Experimental Mechanics (2017). https://doi.org/10.1007/s11340-017-0348-1

[43] Wang, Z., Wu, H., Kang, K., Wang, S., Li, Y., Hou, W., Riaz, H., Li, L., Li, C.: DIC/Moiré hybrid method based on regular patterns for deformation measurement. Optics Express **27**(13), 18435–18444 (2019). https://doi.org/10.1364/OE.27.018435

[44] Semin, B., Auradou, H., François, M.L.M.: Accurate measurement of curvilinear shapes by virtual image correlation. European Physical Journal Applied Physics **56**(1), 10701 (2011). https://doi.org/10.1051/epjap/2011110275

[45] Tong, W.: Formulation of lucas–kanade digital image correlation algorithms for non-contact deformation measurements: A review. Strain **49**(4), 313–334 (2013). https://doi.org/10.1111/str.12039

[46] Pan, B., Wang, B.: Digital image correlation with enhanced accuracy and efficiency: A comparison of two subpixel registration algorithms. Experimental Mechanics **56**(8), 1395–1409 (2016). https://doi.org/10.1007/s11340-016-0180-z

[47] Sur, F., Blaysat, B., Grédiac, M.: Determining displacement and strain maps immune from aliasing effect with the grid method. Optics and Lasers in Engineering **86**, 317–328 (2016) https://arxiv.org/abs/hal-01352868.

https://doi.org/10.1016/j.optlaseng.2016.06.010

[48] Reu, P.: All about speckles: Aliasing. Experimental Techniques **38**(5), 1–3 (2014). https://doi.org/10.1111/ext.12111

[49] Herráez, M.A., Burton, D.R., Lalor, M.J., Gdeisat, M.A.: Fast two-dimensional phase-unwrapping algorithm based on sorting by reliability following a noncontinuous path. Applied Optics **41**(35), 7437–7444 (2002). https://doi.org/10.1364/ao.41.007437

[50] Mullen, M.: 2D and 3D Phase Unwrapping Using SRNCP. https://github.com/mfmullen/PhaseUnwrapping

[51] Sur, F., Blaysat, B., Grédiac, M.: Rendering deformed speckle images with a boolean model. Journal of Mathematical Imaging and Vision **60**(5), 634–650 (2018) https://arxiv.org/abs/hal-01664997. https://doi.org/10.1007/s10851-017-0779-4

[52] Grédiac, M., Blaysat, B., Sur, F.: A critical comparison of some metrological parameters characterizing Local Digital Image Correlation and Grid Method. Experimental Mechanics **57**(6), 871–903 (2017) https://arxiv.org/abs/hal-01509611. https://doi.org/10.1007/s11340-017-0279-x

[53] Grédiac, M., Sur, F., Badulescu, C., Mathias, J.-D.: Using deconvolution to improve the metrological performance of the grid method. Optics and Lasers in Engineering **51**(6), 716–734 (2013). https://doi.org/10.1016/j.optlaseng.2013.01.009

[54] Piro, J.L., Grédiac, M.: Producing and transferring low-spatial-frequency grids for measuring displacement fields with moiré and grid methods. Experimental Techniques **28**(4), 23–26 (2004)

[55] JCGM Member Organizations: International Vocabulary of Metrology – Basic and General Concepts and Associated Terms (VIM) vol. 200. BIPM,

(2012)

[56] Chrysochoos, A., Surrel, Y.: Chapter 1. Basics of metrology and introduction to techniques. In: Grédiac, M., Hild, F. (eds.) Full-field Measurements and Identification in Solid Mechanics, pp. 1–29. Wiley, (2012)

[57] Wittevrongel, L., Lava, P., Lomov, S.V., Debruyne, D.: A self adaptive global digital image correlation algorithm. Experimental Mechanics **55**(2), 361–378 (2015). https://doi.org/10.1007/s11340-014-9946-3

[58] Bornert, M., Brémand, F., Doumalin, P., Dupré, J.C., Fazzini, M., Grédiac, M., Hild, F., Mistou, S., Molimard, J., Orteu, J.J., Robert, L., Surrel, Y., Vacher, P., Wattrisse, B.: Assessment of digital image correlation measurement errors: Methodology and results. Experimental Mechanics **49**, 353–370 (2009). https://doi.org/10.1007/s11340-008-9204-7

[59] iDICs - DIC Challenge. https://idics.org/challenge/

[60] Blaber, J., Adair, B., Antoniou, A.: Ncorr: Open-source 2d digital image correlation matlab software. Experimental Mechanics **55**(6), 1105–1122 (2015). https://doi.org/10.1007/s11340-015-0009-1

A Appendix: vocabulary and definitions

Three metrological parameters are discussed in this paper, namely the *measurement resolution*, the *bias* and the *spatial resolution*. Their definition, already given in [39, 52], are recalled below for the sake of complitness:

- Measurement resolution: in Ref. [55], the measurement resolution is defined by the *smallest change in a quantity being measured that causes a perceptible change in the corresponding indication*. More precisely, it is proposed in [56] to define it as the *change in quantity being measured that causes a change in the corresponding indication greater than one standard deviation*

of the measurement noise, which enables us to quantify the measurement resolution. This definition is quite arbitrary, any other (reasonable) multiple of the standard deviation being also potentially acceptable, but the idea is that the resolution quantifies the smallest change not likely to be caused by measurement noise [56].

- Spatial resolution: the spatial resolution denoted by ℓ_λ is defined here by *the lowest period of a sinusoidal deformation that the technique is able to reproduce before losing a certain percentage* λ *of amplitude*, this quantity being chosen *a priori* [57]. The advantage of this definition is that it is not based on an arbitrary value for the subset size in Local DIC or for the elements size in Global DIC. This makes it possible to compare the spatial resolution between these two techniques.
- Bias:a systematic error generally occurs when a given technique returns actual details in displacement and strain maps. It is due to the fact that the amplitude of such apparent details is generally lower than the amplitude of the actual detail. This apparent "damping" is a bias, which can be quantified by considering a sinusoidal reference displacement field, and measuring the relative loss of amplitude exhibited by the displacement field returned by the technique under study, as suggested in Refs. [57–60]. Of course, the loss of amplitude depends on the frequency f of the sine function. This loss of amplitude is denoted here by $l(f)$. In this context, the spatial resolution defined above is defined for a given bias λ, the relation between ℓ_λ and λ being that ℓ_λ is the smallest value such that $l(1/\ell_\lambda) = \lambda$. We call here λ the bias of the method. This is a slight abuse of language since fixing λ does not mean that the damping of any displacement or strain field is actually equal to this λ value. Note finally that for DIC, the effect quantified here by λ is often referred to as the "matching bias", because it occurs when there is a mismatch between the subset shape function used to describe the displacement within subsets on the one hand, and the degree of the actual displacement if the latter is described by a polynomial on the other hand.

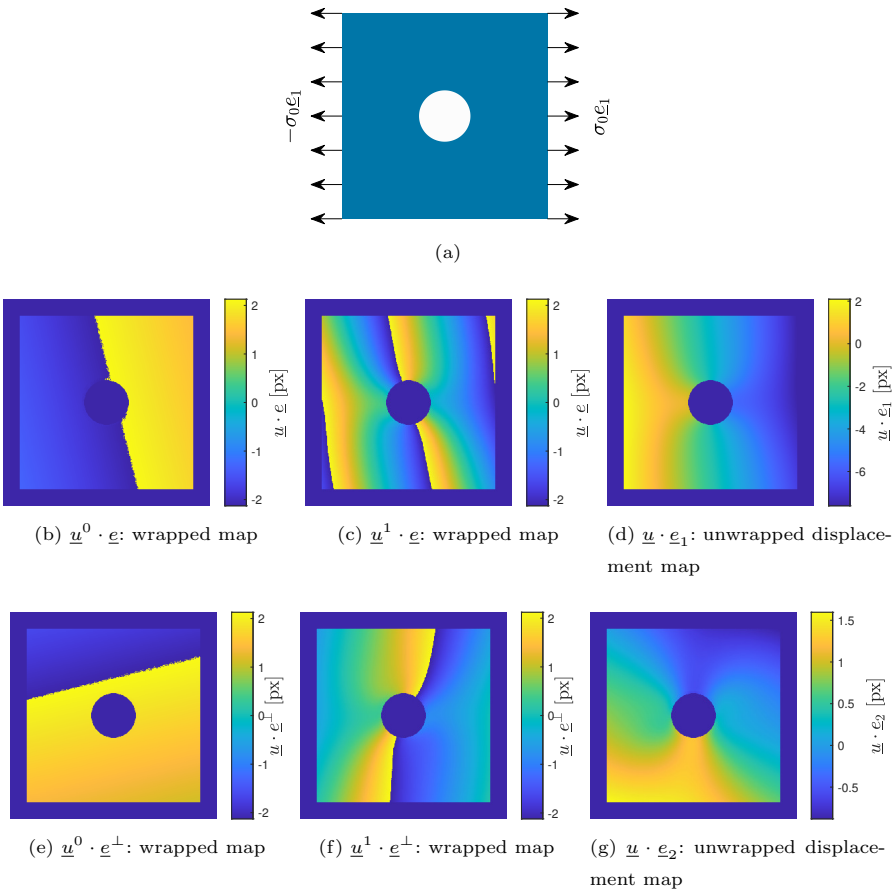

(a)

(b) $\underline{u}^0 \cdot \underline{e}$: wrapped map

(c) $\underline{u}^1 \cdot \underline{e}$: wrapped map

(d) $\underline{u} \cdot \underline{e}_1$: unwrapped displacement map

(e) $\underline{u}^0 \cdot \underline{e}^\perp$: wrapped map

(f) $\underline{u}^1 \cdot \underline{e}^\perp$: wrapped map

(g) $\underline{u} \cdot \underline{e}_2$: unwrapped displacement map

Fig. 7: Hole in an infinite plate case. (a) Schematic representation of the holed (infinite) plate submitted to tension. A closed-form expression of the displacement field of this problem exists, see Equation (14). This displacement is used for generating a pair of synthetic images of a checkerboard, on which Virtual DIC is applied. (b, c, e &f) wrapped displacement fields retrieved by Virtual DIC, which correspond to the reference image (b&e) and the current image (c&f). (d&g) unwrapped displacement fields.

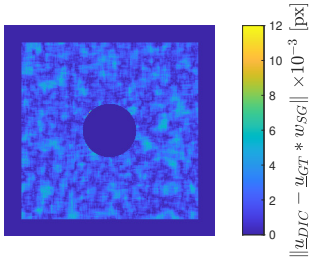

(a) Error between the best solution and DIC output

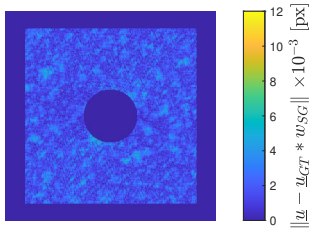

(b) Error between the best solution and Virtual DIC output

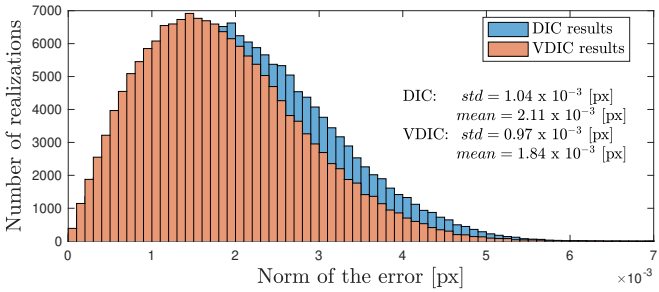

(c) Histograms of the errors

Fig. 8: (a&b) maps of the error between measured displacement fields and the best possible measurement, defined here as the ground displacement convolved with a Savitzky-Golay kernel of width set to subset one, and of the same order as subset shape functions. Errors correspond to the norm of the difference between retrieved displacements by DIC (a) or Virtual DIC (b) and the ground-truth displacement convolved with the Savitzky-Golay kernel. (c) illustrates histograms of the same results. Error of the measurements obtained with Virtual DIC is slightly smaller and less scattered.

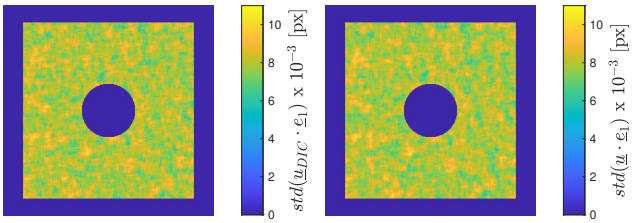

(a) Measurement resolution of DIC along direction $\underline{e}_1$

(b) Measurement resolution of Virtual DIC along direction $\underline{e}_1$

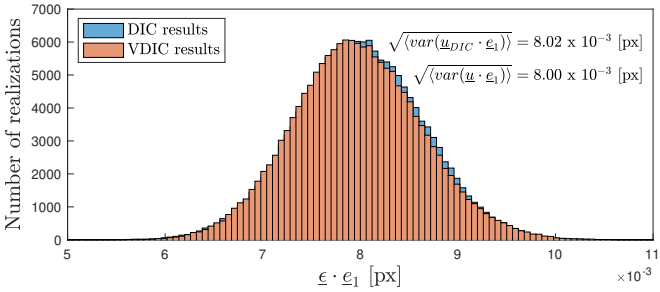

(c) Histograms of data of maps (a) & (b)

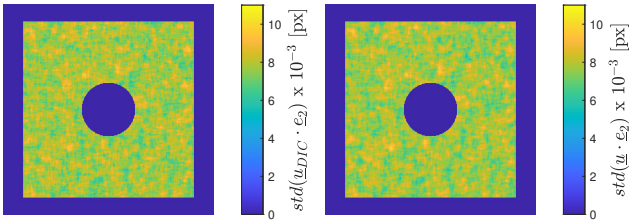

(d) Measurement resolution of DIC along direction $\underline{e}_2$

(e) Measurement resolution of Virtual DIC along direction $\underline{e}_2$

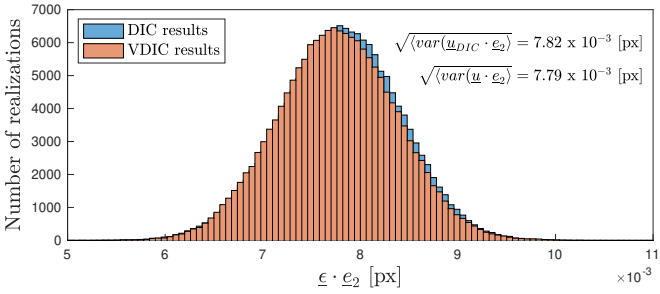

(f) Histograms of data of maps (d) & (e)

Fig. 9: Measurement resolution of DIC and Virtual DIC. 100 pairs of noisy synthetic images are used for computing the measurement resolution obtained with each technique. Noise propagates similarly within DIC and Virtual DIC algorithms.

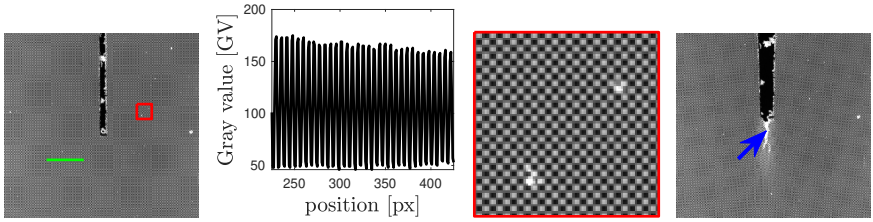

(a) Reference image I^0 (b) Evolution along the green line of (a) (c) Closeup of the red square of (a) (d) Current image I^1

Fig. 10: Experimental tensile test applied to an aluminum open-hole specimen. (a) reference image; (b) evolution of the gray level distribution along the green line of (a); (b) closeup view of the red square of (a); (b) & (c) highlight the difference between the considered pattern and perfect checkerboards; (d) current image. Note the fracture process that highly deteriorates the checkerboard pattern (blue arrow).

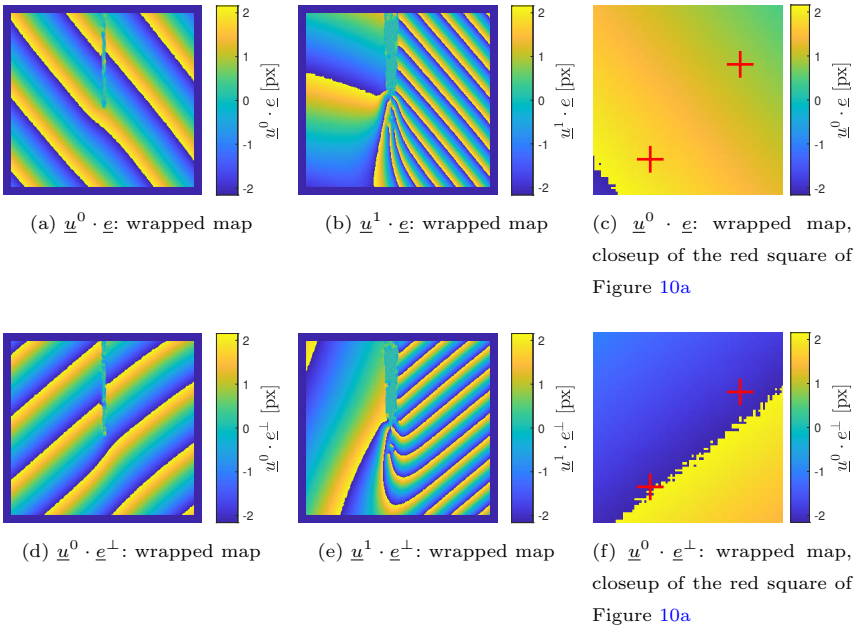

(a) $\underline{u}^0 \cdot \underline{e}$: wrapped map

(b) $\underline{u}^1 \cdot \underline{e}$: wrapped map

(c) $\underline{u}^0 \cdot \underline{e}$: wrapped map, closeup of the red square of Figure 10a

(d) $\underline{u}^0 \cdot \underline{e}^\perp$: wrapped map

(e) $\underline{u}^1 \cdot \underline{e}^\perp$: wrapped map

(f) $\underline{u}^0 \cdot \underline{e}^\perp$: wrapped map, closeup of the red square of Figure 10a

Fig. 11: Displacement maps retrieved by the Virtual DIC technique. First column, *i.e.* (a) & (d), correspond to the components of the wrapped displacement field of the reference state. Second column, *i.e.* (b) & (e), correspond to the components of the wrapped displacement field of the current state. Third column, *i.e.* (c) & (f), correspond to a closeup view of the components of the wrapped displacement field of the reference state in the red square of Figure 10a. The local marking defects observed in Figure 10c do not induce any disruption in the displacement maps (c) & (f). Note that these pattern defects do not affect displacement measurement.

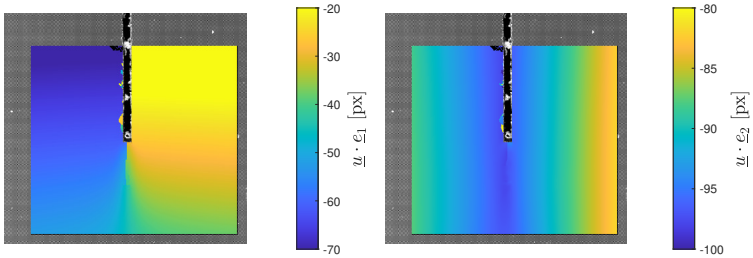

(a) $\underline{u} \cdot \underline{e}_1$: retrievied displacement map (b) $\underline{u} \cdot \underline{e}_2$: retrieved displacement map

Fig. 12: Displacement maps retrieved by the Virtual DIC technique.